Competition between slow slip and damage on and off faults revealed in 4D synchrotron imaging experiments

François Renard[1,2], Jessica McBeck[1], Benoît Cordonnier[1]

[1] Physics of Geological Processes, The Njord Centre, Department of Geosciences, University of Oslo, Oslo, Norway.
[2] University Grenoble Alpes, University Savoie Mont Blanc, CNRS, IRD, IFSTTAR, ISTerre, 38000 Grenoble, France.

Key points

- Dynamic synchrotron imaging characterizes slow slip along pre-existing faults
- Initial fault roughness controls damage production in the volume during slow slip
- Slip on a rough preexisting fault and increasing differential stress induce failure of new faults oriented at high angles

Graphical abstract

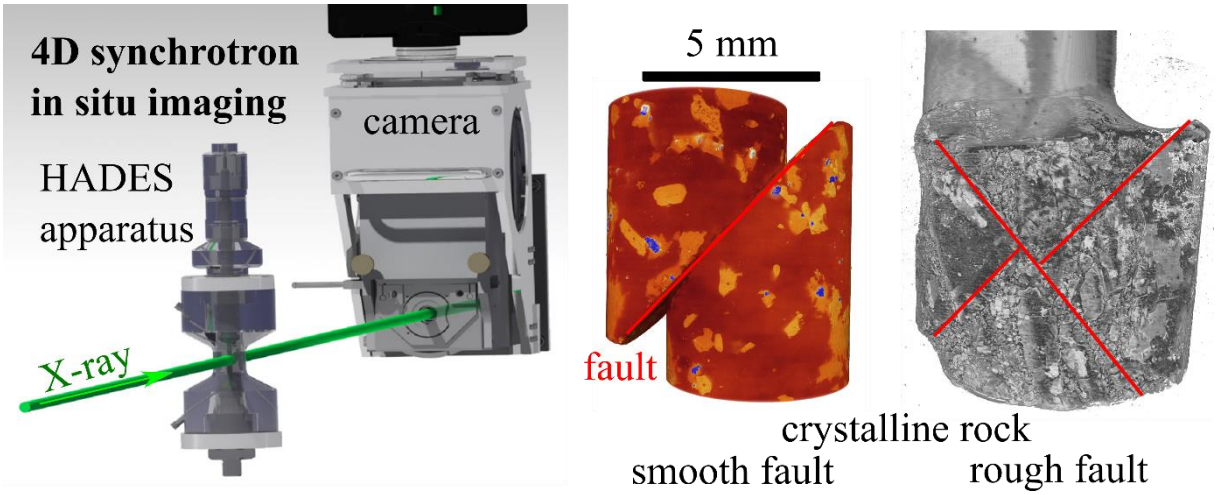

Abstract

In the continental crust, faults may accommodate deformation through aseismic creep, slow slip events, or seismic slips that produce dynamic damage, or a combination of these endmembers. A variety of parameters controls the occurrence of these mechanical behaviors. In a series of laboratory experiments, we image centimeter-scale faults during sliding under *in situ* conditions. We perform four experiments of slip on centimeter-scale crystalline rock samples prepared with a saw-cut interface at 45° from the direction to the maximum compressive stress and at stress conditions of 2-3 km depth. We image fault slip and off-fault fracture development using 4D synchrotron X-ray microtomography. Three faults have an initial rough interface, and deformation occurs with increasing differential stress by a combination of slow slip events and off-fault damage, until catastrophic failure and the formation of new faults. Conversely, the pre-cut fault with a smooth initial surface deforms mainly by slow slip, develops numerous striations along its slip plane, and no microfractures are detected in the wall rock. Our experiments reproduce aseismic and seismic faulting behavior, and demonstrate that the roughness of the fault plane is one of the parameters that control the transition between these two behaviors. A fault with a rougher interface may tend to develop more off-fault damage and seismic behavior. For the rough fault experiments, the secondary faulting occurs along a network of faults oriented at high angles from the pre-existing saw-cut plane, a behavior similar to several earthquake sequences that occurred along orthogonal faults.

1. Introduction

Two endmember modes of slip occur on continental faults depending on whether a rupture propagates at a velocity close to that of the elastic waves in the crust, in the case of earthquakes, or at slower velocities, without producing dynamic elastic effects. In the second case, the ruptures are described as slow slip events, when the slip occurs episodically and slower than seismic slip, and creep when the slip is continuous and slow (e.g., Bürgmann, 2018). These slow deformations are recorded by geodetic and field measurements such as creepmeters. They may be accompanied by tremor signals recorded by seismometers. Several parameters could explain the transition between these two behaviors, including the tectonic loading rate, rock material properties, initial stress on the fault, or fluid pressure (Bürgmann, 2018).

The energy budget of tectonic systems includes on- and off-fault energy dissipation. Natural observations show that damage and secondary faults develop in the volume near active faults and evolve with slip (e.g. Ben-Zion and Sammis, 2003; Griffith et al., 2010; Choi et al., 2016). Field observations show that dynamic ruptures during earthquakes produce damage. However, only laboratory experiments have thus far shown the existence of damage formation and secondary faulting during slow slip (French and Zhu, 2017). Seismological observations indicate the presence of microseismicity in a large volume around the main faults in southern California (Ross et al., 2017). In addition, complex strain partitioning has occurred in a few earthquake sequences in the past decades, where two successive major earthquakes nucleated on two faults with orthogonal orientations (Hudnut et al., 1989; Yue et al., 2012; Ross et al., 2019). These observations suggest the existence of strain partitioning between the main faults and the surrounding volume during fast or slow slip. However, how precursory strain partitioning may control earthquake nucleation remains unconstrained.

Field observations show that fault surfaces are rough at all scales (Power et al., 1987; Renard et al., 2006; Sagy et al., 2007; Renard et al., 2013). This roughness promotes the concentration of local stresses during slip, which then increases the shear strain in a volume surrounding the principal slip zone (Sagy and Lyakhovsky, 2019), leading to off-fault damage development. A damage zone develops progressively with cumulated slip by a combination of dynamic fracturing during earthquake propagation, creation of surface area by microseismicity, and slow slip. This process leads to an evolving energy budget between energy dissipation on the fault and dissipation in the volume. In a previous study (McBeck et al., 2019), we calculated that the energy dissipated on precut fault planes in X-ray tomography experiments dominates the other work components, and may reach nearly 100% of the external work imposed on the samples. Conversely, between 5 and 20% of the external work dissipates as off-fault deformation when fractures develop in the volume around the fault. Moreover, we document that with cumulated slip, the partitioning of the energy budget evolves as off-fault damage propagates.

In the present study, we perform a series of laboratory experiments on crystalline rock samples that contain a preexisting saw-cut fault plane with an imposed initial roughness. We deform the samples under *in-situ* conditions of 2-3 km depth and reproduce slow slip deformation along the faults while imaging the sample using dynamic synchrotron X-ray microtomography. By varying the initial fault roughness and keeping all other experimental parameters constant, we reproduce two mechanical behaviors: reactivation of the preexisting fault with no detected off-fault damage, or reactivation with detected off-fault damage and secondary faulting. Here, our main goal is to demonstrate that slow slip on a fault may produce damage in the surrounding volume, and that the accumulation of this damage may lead to the nucleation of a laboratory earthquake that forms on a fault oriented at a high angle from the preexisting saw-cut fault. Under similar experimental conditions, and for a similar

amount of total slip in the range 1-2.5 mm, a smooth fault does not develop detected off-fault damage, in contrast to a rougher fault.

2. Methods

2.1 Material and sample preparation

The rock samples are made of monzonite, a crystalline rock with grain size of 450 micrometers described in Aben et al. (2016), and used in Renard et al., (2018) and McBeck et al. (2019). From a single monzonite block, we cored four cylinders, with 5 mm diameter and 10 mm height. Then, a plane was cut with a diamond string saw at 45° from the flat surfaces of the cores, to represent an initial fault oriented at 45° from the direction of the main compressive stress, σ_1. The angle of 45° is within the range 30-50° where experiments have shown fault reactivation (Giorgetti et al., 2019). Moreover, the orientation of 45° allowed greater total slip than 30° in our experimental apparatus. The four fault surfaces were polished with sandpapers from P800 to P4000 grit, producing a smooth mirror-like surface. The initial topography of the fault was measured using a white light interferometer (ContourGT, Bruker) over a 1.7 x 1.3 mm^2 surface area. Here, we define the roughness, S_q, by the root mean square of the height $z(x,y)$ over the surface area A, $S_q = \sqrt{\frac{1}{A}\iint_A z^2(x,y)\,dxdy}$ and, before slip, S_q = 0.6 μm. The value falls in the range of wavelengths of white light (0.4-0.7 μm), which explains why the initial surface was shiny and mirror-like because of the specular reflection. One of such smooth samples, representative of a smooth fault surface, was kept for experimental deformation. For the three other samples representative of a rough fault surface, the fault surface was roughened with ten passes of P400 sandpaper, and three passes of P80 sandpaper. Passes were applied perpendicularly to the slip direction such that slip would enhance interlocking of the fault. This procedure produces feature analogous to natural situations that are not parallel to the present slip direction due to a background stress rotation,

for example. This procedure also creates roughness anisotropy, which is observed on most fault surfaces (e.g., Renard et al., 2006). The root-mean-square roughness for the three samples with a rough fault was S_q=4.9 μm, about eight times higher than that of the smooth fault (0.6 μm). We prepared all samples at once to ensure a good reproducibility.

2.2 Experimental conditions

The experimental procedure is described in McBeck et al. (2019) and summarized here. The samples called M6 and M8 in McBeck et al. (2019) are the same as the samples MONZ6C and MONZ8C in the present study, which contains data of two additional experiments, MONZ9C and MONZ10C. Table 1 indicates the experimental conditions for the four samples. Figures 1 and S1 show the time evolution of the control parameters and fault slip calculated from the loading displacement. Time-lapse images of fault slip and damage are provided as Supplementary Information (Movies S1, S2, S3, and S4).

Each sample was encased in a Viton jacket that was placed between two stainless steel pistons. The sample assembly was inserted in the triaxial deformation apparatus HADES installed on the microtomography beamline ID19 at the European Synchrotron Radiation Facility. This apparatus was described in detail in previous studies (Renard et al., 2016; 2017). In short, the axial and confining pressures are controlled by two separate pumps which have a pressure resolution of 0.1 MPa. The confining medium is oil. The axial stress on the sample is controlled by increasing the oil pressure in the axial load chamber of the apparatus. The interfaces between the sample and the pistons were not lubricated; however, some slip occurred along these interfaces during experiments, as seen in supplementary movies (Movies S1 and S4).

We performed all experiments at room temperature, with no fluid inside the sample. First, equal confining and axial stresses were applied on the sample assembly before the first X-ray

tomography scan was acquired. Then, the axial stress was increased slowly and by successive steps until an increment of slip of 50 to 100 micrometers was measured. This vertical distance was measured from the Linear Variable Differential Transformer (LVDT) displacement sensor located outside of the rig, corrected from the elasticity of the rig, and then was projected along the fault slip direction. Using the 3D images, we measured the shortening of the sample and obtained the same displacement values as those of the LVDT. In all experiments, the slip increments occurred with a slow velocity, similar to slow slip events (see insets in Figure 1a, c, d). After each stress step increase and slip increment, one 3D X-ray tomogram was acquired. For samples MONZ6C and MONZ10C, the axial stress was reduced before each scan (red curves in Figures 1a, e) as we anticipated that some small creep could occur on the fault if the stress was maintained constant, potentially producing blurry tomograms. For samples MONZ8C and MONZ9C, we did not follow this procedure and had to remove several tomograms that were blurred. For sample MONZ8C, the initial confining pressure was 50 MPa and the axial stress was increased to 200 MPa, the upper limit of the HADES rig, without significant slip on the fault. Consequently, we had to reduce the confining pressure to first 30 MPa and then 10 MPa to allow more slip (Figure 1c). For the other three samples, the confining stress remained constant over the experiments.

For all the samples, as slip accumulated on the fault, a space formed between the jacket surrounding the sample and the offset fault plane. This space has the shape of an annulus around the fault zone with a thickness close to 1 mm. Consequently, the confined pressure applied near the fault was smaller than on the rest of the core sample. Another consequence of our experimental set-up is that, as the fault slips, torque develops on the upper and lower pistons and the sample rotates in the rig along a horizontal axis, with an angle smaller than 3°. We consider these effects to have a similar impact in all experiments in terms of boundary

conditions applied to the sample, such that the differences measured between experiments are influenced by these boundary conditions to the same degree.

Between 5 and 42 tomograms were acquired in each experiment, with a voxel size of 6.5 μm and a spatial resolution close to the voxel size. The exposure time was 0.05 s, the beam energy reaching the sample was 85 keV, and 1600 projections were taken over 180°, resulting in a total scan time per acquired volume of about 2 min. Each experiment lasted between one and six hours. Tomographic reconstruction was performed using the program PyHST2 (Mirone et al., 2014). The tomograms map the three-dimensional X-ray attenuation in the samples, with more dense minerals having a stronger attenuation than lighter minerals or air filling voids.

For sample MONZ9C, only five tomograms could be acquired because a secondary fault formed after a displacement of 890 μm, a total displacement only 50% of the two other rough fault samples, for which the total slip was around 2 mm before secondary faulting (Table 1).

At the end of each experiment, the sample was removed from the rig. Sample MONZ6C was intact, and so the fault surface was coated with 10 nm gold and imaged using scanning electron microscopy (Hitachi SU5000 FE-SEM, Department of Geosciences, University of Oslo). Its topography was measured using white light interferometry. The other samples were destroyed when removed from the rig and so could not be characterized further.

The experiment MONZ6C, with a smooth fault, was performed to verify that a fault would produce only slow slip events under the imposed stress conditions. The three other experiments were performed to demonstrate that, under increasing differential stress conditions, slow slip could produce damage in the volume and lead to secondary seismic faulting. Despite the different confining pressures, these three experiments show reproducible results.

3. Results

3.1 Stress and strain versus displacement

For all experiments, the macroscopic shear strength increased with cumulated displacement because it became necessary to apply larger axial stress to trigger slip (Figure 1 b, d, f, S1). Two main deformation behaviors occurred (Figure 2): either continuous slip along the saw-cut fault (MONZ6C), or synchronous slip along the saw-cut fault and damage development in the volume, leading to secondary faulting in the three other experiments. We quantified these two deformation modes using Digital Volume Correlation analysis on pairs of tomograms of samples MONZ6C and MONZ8C in a previous study (McBeck et al., 2019). Here, we focus on the porosity evolution and fracture development in the samples during slip on the preexisting fault.

For the smooth fault (MONZ6C), slow slip events occurred at each stress increase and no detected damage developed in the volume (Figures 1b, 2a, Movie S1). Some porosity was initially present in the fault plane. These small pores could be tracked throughout the experiment, as well as off-fault pores. The pores in the lower part of the sample did not change location; and the pores in the upper part of the sample moved with slip (Movie S1, left panel).

For sample MONZ8C, the confining pressure was changed twice in order to increase the differential stress after the apparatus reached its axial stress limit. During slip, some minerals were sheared along the fault plane and material was dragged into this plane (2D views, top right in Movie S2). Microfractures nucleated and grew in the volume around the fault (Movies S2, S3) and tomography data allow detecting the opening (tensile component) of these microfractures because of the change in density contrast between air in open voids (pores) and minerals. The first microfracture opened as a tensile crack that nucleated from the fault surface and at an angle almost perpendicular to the fault, and then propagated away from

194 it (Movie S3). Damage development was highly asymmetric. Tensile microfractures grew
195 mainly in the rock block in contact with the upper piston, which was moving down to apply
196 the load (Movie S3). Microfractures nucleated either from the fault surface or in the rock
197 volume and then generally propagated until reaching the fault surface. After significant
198 damage accumulation, several microfractures became connected in three dimensions. The
199 sample failed along secondary faults (Figure 2b). This failure produced a significant stress
200 drop, within less than one second, which the servo-control of the triaxial apparatus could not
201 equilibrate. Because of the short duration of this event, we suggest it was seismic. The
202 HADES triaxial apparatus is not equipped with acoustic emission recording that could verify
203 this seismic behavior.

204 Samples MONZ9C (Figure S2) and MONZ10 C (Movie S4) behaved similarly to sample
205 MONZ8C, including the production of damage and secondary faulting on a fault oriented at a
206 high angle to the preexisting fault and a sudden stress drop at macroscopic failure, potentially
207 indicative of seismic behavior. For sample MONZ9C, we acquired too few tomograms to
208 allow characterizing damage development with sufficient detail. For sample MONZ10C, the
209 first damage occurred as a tensile microfracture that nucleated from the fault surface, with a
210 similar behavior to sample MONZ8C. Then this microfracture propagated away from the
211 saw-cut fault and rotated toward the direction of σ_1 (dashed arrow in Figure 2).
212 Microfractures developed in the volume on both sides of the fault, until the sample failed
213 along a newly created fault (Movie S4, Figure 2b), with a measurable stress drop that
214 occurred within less than one second.

215 To summarize, the results show that the smooth fault slipped without creating measurable
216 damage in the volume, whereas, for the three rough fault samples, tensile microfractures
217 nucleated from the fault surface or directly in the volume, grew and became interconnected,
218 until the sample failed catastrophically along a newly created fault.

3.2 Striation development on the smooth fault

We imaged the fault surface of sample MONZ6C (the smoother initial fault) using scanning electron microscopy and white light interferometry (Figure 3). Initially, the fault surface was smooth and mirror-like. After the experiment, the fault surface was still shiny and no damage could be detected by eye. However, high-resolution imaging and topography measurements demonstrate that striations developed in the direction of slip, with sub-micrometer to micrometer amplitude (Figure 3). The striations cross several minerals over the entire fault surface. At the tip of some striations, small particles appear concentrated (Figure 3c), likely through a mechanical ploughing process. Many of these particles also accumulated in the lower topography (e.g., valleys) of the surface (Figure 3d), creating a discontinuous gouge layer (white rectangle in Figure 3d). The development of striations with slip reduced the initial roughness from S_q = 0.6 μm before slip to S_q = 0.3 μm at the end of experiment.

3.3 Porosity, damage and secondary faulting on rough faults

In the three samples with a rough fault, slow slip along the preexisting saw-cut fault produced damage in the surrounding volume. In two samples (MONZ8C, MONZ10C), the first microfracture nucleated from the initial saw-cut fault and then propagated in the volume. Its main plane rotated in the direction of σ_1 (Movies S3, S4). Other microfractures developed in the volume and nucleated at some distance from the saw-cut fault (Figures 4). Most microfractures were transgranular.

The development of damage in the wall rock was heterogeneous in space and time (Figure 5). It occurred by the nucleation and growth of microfractures, detected as voids in the tomograms. Because of the specificity of the experimental setup, an annulus of voids formed around the fault zone due to the fault off-set at the core boundaries and resulting detachment

244 of the jacket (Movies S3 and S4).Therefore, the number of void voxels detected near the fault
245 plane does not reflect the true porosity on the fault plane (blue rectangles in Figure 5). Here,
246 we focus on off-fault damage, and do not consider the number of voxels detected near the
247 plane. Outside of this zone, damage developed in the wall rock as microfractures initiated,
248 grew and merged. Damage development was highly heterogeneous and developed only on
249 one side of the saw-cut fault for sample MONZ8C (Figure 5 a, c), whereas it developed on
250 both sides for sample MONZ10C with an asymmetric distribution (Figure 5 b, d).
251 In the smooth fault experiment, microporosity initially present in the sample corresponded
252 either to pores in feldspar minerals or pores initially present along the fault plane. We
253 extracted the pores in the fault plane by cropping a subvolume around the fault in the
254 tomogram that excluded the sides of the fault where some artefact porosity arises from the
255 separation between the jacket and the sample. With cumulated slip, the total volume of these
256 pores remained constant, close to a value of $2 \cdot 10^{-12}$ m^3, corresponding to a volume fraction of
257 $3 \cdot 10^{-6}$ when dividing by the sample volume (Figure 6a). Conversely, for the rough faults,
258 damage developed with slip and, for sample MONZ10C, the total volume of voids before the
259 sudden stress drop that led to failure was $4 \cdot 10^{-10}$ m^3, corresponding to a volume fraction of
260 $5 \cdot 10^{-4}$. This volume fraction increased with cumulated slip because of the growth of
261 microfractures and, just before macroscopic failure, it was more than two orders of magnitude
262 larger than for the smooth sample (Figure 6b).
263 Microfractures detected in the tomograms must have hosted a tensile component because
264 only fractures with apertures larger than the spatial resolution of the tomograms may be
265 observed. Some microfractures may have hosted a shear component due to local rotations
266 when nearby microfractures opened simultaneously or when a microfracture was not planar,
267 and contained kinks. Before the sudden stress drop that led to the final failure of the samples
268 with rough faults, several microfractures became interconnected and formed clusters

connected in three-dimensions. This secondary fault network formed with a sudden stress drop and was presumably seismic. In the three samples where it occurred, this network had an angle to the original surface in the range 75-85° (e.g., Figures 2b, S2, and last image in Movie S4).

4. Discussion

4.1 Deformation on the fault plane

During slip, asperities may flatten, leading to an increase in actual contact area and a strengthening of the interface (Scholz and Engelder, 1976). The drag of these asperities along the surface produces mechanical wear and striations (Power et al., 1987), revealed in shear experiments on salt (Renard et al., 2012). The saw-cut fault interface strengthens in our experiments, as the shear stress necessary to trigger slow slip increases with displacement (Figure 1, a, c, e). Deformation along the interface occurs through the formation of striations, the ploughing of asperities, and grain comminution (Figure 3). The first two processes could explain the increasing strength, as they overcome the weakening effect of gouge formation (Reches and Lockner, 2010). For the rough faults, damage first nucleates from the fault surface for two samples (MONZ8C and MONZ10C). We infer that these microfractures could open because of local tensile stress near an asperity on the fault surface, from which microfractures could nucleate and propagate in the volume around the fault.

4.2 Damage development and secondary faulting

In a previous study, we performed Digital Volume Correlation to calculate the evolution of incremental strain during slip on the preexisting fault (McBeck et al., 2019). For the smooth fault (sample MONZ6C), almost 100% of the external work was dissipated by frictional slip along the precut interface, and the fault zone width did not broaden with

cumulated slip. For the rough fault (sample MONZ8C), damage zone development lead to higher values of strain energy density. This strain energy was consumed in the formation of off-fault damage, and the energy dissipated in frictional slip decreased relative to the smooth fault experiment. A low amount of energy dissipated by off-fault damage was also identified in a series of *in situ* rotary shear X-ray microtomography experiments performed on cement mortar (Zhao et al., 2020). This study imaged the development of off-fault damage and found that the fracture energy produced by this damage was less than 0.3% of the total energy budget, in agreement with experiments where a fault propagated subcritically and created damage at its tip (Aben et al., 2019).

In our experiments with rough faults, the secondary shear faults develop due to the increasing number of tensile transgranular microfractures, and the coalescence of these microfractures, with dilatancy preceding observed shear displacement (Figures 4, 5, Movies S3, S4). This behavior is similar to the rupture of rock samples that do not include a pre-existing saw-cut fault (Brace et al., 1966; Peng and Johnson, 1972; Reches and Lockner, 1994; Lei et al., 2000; Renard et al. 2018; Aben et al., 2019), and the faulting of rock samples in which a pre-existing fault is not optimally oriented (Jackson and Dune, 1974; Giorgetti et al., 2019) or is deformed in a rotary shear apparatus (Zhao et al., 2018; 2020). Analytical calculations and experiments indicate that for pre-existing faults oriented at 45° from σ_1, fault reactivation may occur (Sibson, 1985) and that this angle is located near a transition where one could observe either reactivation or off-fault fracture (Giorgetti et al., 2019).

Numerical simulations of dynamic rupture indicate that the distribution of off-fault damage depends on the angle between the preexisting fault and the loading direction (Poliakov et al., 2002; Xu and Ben-Zion, 2013). In these simulations, off-fault damage occurs because the stress in the volume around the fault reaches the plastic limit of the material during the propagation of a dynamic rupture. Secondary shear faulting at a high angle to the

main fault may form during rupture deceleration (Xu and Ben-Zion, 2013) or because fault topography is rough and leads to the concentration of elastic and plastic strain in the volume (Dunham et al., 2011; Sagy and Lyakhovski, 2019). In contrast, in our experiments slip on the saw-cut fault occurs as slow slip (insets in Figures 1 a, c, e) and off-fault damage is therefore produced during quasi-static (slow) slip along the main fault. Secondary faulting in our experiments could be reminiscent of antithetic Riedel R' shear bands (Riedel, 1929) that form at an angle of 75° from the main displacement surface (e.g., Figure 2 in Davis et al., 2000). However, Riedel patterns nucleate and grow from the tip of a fault during its propagation, whereas in our experiments, microfractures nucleate from the fault surface or in the surrounding volume. The interlocking of asperities on the fault plane creates stress perturbations, which generate the microfractures.

Laboratory experiments on serpentines produced off-fault damage during slow slip (French and Zhu, 2017). These experiments used fluid pressure to control the development of slow ruptures. They produced secondary shear fractures at a high angle to the main fault surface, with a final fast dynamic rupture triggered by the strain-weakening of microfracture development. We also observe such a process. However, as there was no fluid in our experiments, we so conclude that slow slip, damage formation, and secondary faulting may also occur under dry conditions.

Fault roughness may control damage development in the surrounding volume for both quasi-static and dynamic slip. The state of stress around a fault varies with the amplitude and scaling of wavelengths of fault roughness (Dietrich and Smith, 2009; Dunham et al., 2011; Sagy and Lyakhovsky, 2019). Tensile microfractures oriented at a high angle from a rough fault segment have also been observed in the field (Griffith et al., 2010), and in the damage zone of non-planar faults (e.g. Choi et al., 2016). In our experiments, fault roughness amplitude controls a transition from slow slip events to secondary faulting. The fault with an

initial smooth surface with 0.6 μm roughness slipped without off-fault damage whereas slip on the faults with an initial roughness of 4.9 μm produced off-fault damage and secondary faulting. The presence of asperities (i.e. rougher parts of the surface) concentrates stress during slip, allowing nucleating tensile microfractures that initiate directly from the saw-cut fault or in the volume around it. Figure 7 shows an evolution of such a process where damage, in the form of tensile microfractures, grow until the sample fails along a secondary fault network oriented at a high angle (> 75°) from the saw-cut fault.

We interpret this high angle as the result of two processes. First, some damage nucleated at a high angle from the initial fault surface, probably near asperities where higher tensile stress was concentrated (e.g., Zhao et al., 2018). However, because the initial roughness of the rough fault was 4.9 μm, below the 6.5 μm spatial resolution of the X-ray tomography data, we cannot identify which asperity led to the formation of these tensile microfractures. Second, the boundary conditions in the experiments, with friction between the pistons and the sample, could produce locally mode III loading, leading to stress rotation in the sample and local tensile stress conditions.

4.3 Secondary faulting in natural environments

Laboratory experiments have shown that strain accommodation zones located between parallel faults may explain the rotation of faults and, in some cases, the formation of secondary faults with angles of 30-90° from the pre-existing fault (e.g., Figure 1 in McClay and White, 1995; Bonini et al., 1997). In these two studies, a direction of extension was an imposed boundary condition and varied during opening of laboratory rifts. In the experiments of the present study, the main direction of deformation remained constant. Therefore, stress rotation that induced secondary faulting results from local effects in the sample, and not from a change in external boundary conditions.

Investigations of fault growth using the shear crack model usually assume propagation from the tip of an existing fault (Segall and Pollard, 1980; Cowie and Scholz, 1992), with the coalescence of tensile microfractures at various orientations at the fault tip (Vermilye and Scholz, 1999). Secondary faulting at various angles from a main principle displacement surface is often described as Riedel structures (Riedel, 1929; Davis et al., 2000). In the field, active faults may show strain partitioning along orthogonal shear planes. For example, the seismicity recorded near the San Jacinto Fault zone, California, shows a distribution along orthogonal faults (Ross et al., 2017). Most earthquakes with a magnitude $M > 4$ occur along pre-existing faults trending the NW-SE, quasi-parallel to the plate boundary. Conversely, abundant microseismicity that contains $M < 2$ earthquakes occurs off-fault or on almost vertical faults trending orthogonally to the plate boundary. These observations show that off-fault damage occurs in the volume around main faults, and could align along almost perpendicular directions in secondary faults, as in our experiments.

Dynamic rupturing along faults oriented perpendicularly to a pre-existing fault has been observed in several cases where, during an earthquake sequence, slip on one fault triggers earthquakes on almost orthogonal faults. During the Superstition Hill sequence in California in 1987, two earthquakes (Ms 6.2 and Ms 6.6) occurred 11.4 hours apart on two faults that were oriented almost perpendicularly. Hudnut et al., (1989) proposed two explanations: 1) slip on one fault could decrease the normal stress on another fault, triggering an earthquake, and 2) a stress diffusion process, presumably mediated by fluids, could explain the delay between the two earthquakes. Strike-slip earthquakes along orthogonal faults has also been observed during the 2012 Wharton Basin earthquake sequence in the Indo-Australian plate (Yue et al., 2012) and the 2019 Ridgecrest sequence in California (Ross et al., 2019). In both cases, two successive large earthquakes occurred on two orthogonal faults with a delay of 40 seconds for the Wharton Basin sequence and 34 hours for the Ridgecrest sequence. These

observations, supported by our experimental results, indicate that damage and stress transfer in the volume around a slipping fault can induce localization and slip on secondary faults oriented at a high angle to the main fault.

5. Conclusions

Using dynamic synchrotron microtomography imaging of crystalline rocks containing a preexisting fault, under *in situ* stress conditions of of 2-3 km depth, we quantify on- and off-fault damage produced during slow slip. Preexisting faults were oriented at 45° to the maximum compressive stress, and were reactivated during loading. For an initially smooth fault (S_q = 0.6 μm), slip occurred as slow slip events, with the development of mechanical striations on the fault plane and likely rotation of the principal stress directions. Although the interface strengthened with slip, no observed off-fault damage formed. For an initially rough fault (S_q = 4.9 μm), slip occurred as slow slip events and damage developed in the surrounding volume, perhaps due to the locking of asperities on the fault plane. This damage occurred as tensile microfractures whose density and volume increased with slip on the main fault, until a fault network propagated and slipped dynamically at a high angle to the preexisting fault. Our results demonstrate that off-fault damage forms during slow slip, and that its distribution may be asymmetric, even in rocks of the same stiffness. This damage can allow dynamic rupture along secondary faults, as observed in several earthquake sequences that activated dynamic ruptures on orthogonal sets of faults.

Acknowledgements

We thank Elodie Boller, Paul Tafforeau, and Alexander Rack for providing advice on the design of the tomography setup, and Sanchez Technology for building the deformation

418 apparatus. The authors received funding from the Research Council of Norway (grant
419 272217). A dataset with all X-ray tomography data is available (Renard, 2020).

References

Aben, F. M., Doan, M. L., Mitchell, T. M., Toussaint, R., Reuschlé, T., Fondriest, M., Gratier, J.-P., & Renard, F. (2016). Dynamic fracturing by successive coseismic loadings leads to pulverization in active fault zones. Journal of Geophysical Research: Solid Earth, 121(4), 2338-2360.

Aben, F. M., Brantut, N., Mitchell, T. M., & David, E. C. (2019). Rupture Energetics in Crustal Rock From Laboratory-Scale Seismic Tomography. Geophysical Research Letters, 46(13), 7337-7344.

Ben-Zion, Y., & Sammis, C. G. (2003). Characterization of fault zones. Pure and Applied Geophysics, 160(3-4), 677-715.

Brace, W. F., Paulding Jr., B. W., Scholz, C. H. (1966). Dilatancy in the fracture of crystalline rocks, Journal of Geophysical Research, 71, 3939–3953.

Bonini, M., Souriot, T., Boccaletti, M., & Brun, J. P. (1997). Successive orthogonal and oblique extension episodes in a rift zone: Laboratory experiments with application to the Ethiopian Rift. Tectonics, 16(2), 347-362.

Bürgmann, R. (2018). The geophysics, geology and mechanics of slow fault slip. Earth and Planetary Science Letters, 495, 112-134.

Choi, J. H., Edwards, P., Ko, K., & Kim, Y. S. (2016). Definition and classification of fault damage zones: A review and a new methodological approach. Earth-Science Reviews, 152, 70-87.

Cowie, P. A., & Scholz, C. H. (1992). Physical explanation for the displacement-length relationship of faults using a post-yield fracture mechanics model. Journal of Structural Geology, 14(10), 1133-1148.

Davis, G. H., Bump, A. P., García, P. E., & Ahlgren, S. G. (2000). Conjugate Riedel deformation band shear zones. Journal of Structural Geology, 22(2), 169-190.

445 Dieterich, J. H., & Smith, D. E. (2009). Nonplanar faults: Mechanics of slip and off-fault
446 damage. In Mechanics, structure and evolution of fault zones (pp. 1799-1815). Birkhäuser
447 Basel.
448 Dunham, E. M., Belanger, D., Cong, L., & Kozdon, J. E. (2011). Earthquake ruptures with
449 strongly rate-weakening friction and off-fault plasticity, Part 1: Planar faults. Bulletin of the
450 Seismological Society of America, 101(5), 2296-2307.
451 French, M. E., & Zhu, W. (2017). Slow fault propagation in serpentinite under conditions of
452 high pore fluid pressure. Earth and Planetary Science Letters, 473, 131-140.
453 Giorgetti, C., Tesei, T., Scuderi, M. M., & Collettini, C. (2019). Experimental insights into
454 fault reactivation in gouge-filled fault zones. Journal of Geophysical Research: Solid Earth,
455 124, 4189– 4204. doi: 10.1029/2018JB016813.
456 Griffith, W. A., Nielsen, S., Di Toro, G., and Smith, S. A. F. (2010). Rough faults, distributed
457 weakening, and off-fault deformation, Journal of Geophysical Research, 115, B08409,
458 doi:10.1029/2009JB006925.
459 Hudnut, K. W., Seeber, L., & Pacheco, J. (1989). Cross-fault triggering in the November 1987
460 Superstition Hills earthquake sequence, southern California. Geophysical Research Letters,
461 16(2), 199-202.
462 Jackson, R. E., & Dunn, D. E. (1974). Experimental sliding friction and cataclasis of foliated
463 rocks. International Journal of Rock Mechanics and Mining Sciences, 11(6), 235-249.
464 Lei, X., Kusunose, K., Rao, M. V. M. S., Nishizawa, O., & Satoh, T. (2000). Quasi-static fault
465 growth and cracking in homogeneous brittle rock under triaxial compression using acoustic
466 emission monitoring. Journal of Geophysical Research: Solid Earth, 105(B3), 6127-6139.
467 McBeck, J., Cordonnier, B., Mair, K., & Renard, F. (2019). The evolving energy budget of
468 experimental faults within continental crust: Insights from in situ dynamic X-ray
469 microtomography. Journal of Structural Geology, 123, 42-53.

McClay, K. R., & White, M. J. (1995). Analogue modelling of orthogonal and oblique rifting. Marine and Petroleum Geology, 12(2), 137-151.

Mirone, A., Brun, E., Gouillart, E., Tafforeau, P., & Kieffer, J. (2014). The PyHST2 hybrid distributed code for high speed tomographic reconstruction with iterative reconstruction and a priori knowledge capabilities. Nuclear Instruments and Methods in Physics Research Section B: Beam Interactions with Materials and Atoms, 324, 41-48. doi:10.1016/j.nimb.2013.09.030.

Poliakov, A. N. B., Dmowska, R., & Rice, J. R. (2002). Dynamic shear rupture interactions with fault bends and off-axis secondary faulting, Journal of Geophysical Research, 107(B11), 2295, doi:10.1029/2001JB000572.

Peng, S., Johnson, A. M. (1972). Crack growth and faulting in cylindrical specimens of Chelmsford granite. International Journal of Rock Mechanics and Mining Science, 9, 37-86.

Power, W. L., Tullis, T. E., Brown, S. R., Boitnott, G. N., & Scholz, C. H. (1987). Roughness of natural fault surfaces. Geophysical Research Letters, 14(1), 29-32.

Reches, Z. E., & Lockner, D. A. (2010). Fault weakening and earthquake instability by powder lubrication. Nature, 467(7314), 452-455.

Reches, Z., Lockner, D. A. (1994). Nucleation and growth of faults in brittle rocks, Journal of Geophysical Research, 99, 18159-18173.

Renard, F., Voisin, C., Marsan, D., & Schmittbuhl, J. (2006). High resolution 3D laser scanner measurements of a strike-slip fault quantify its morphological anisotropy at all scales, Geophysical Research Letters, 33, L04305, doi:10.1029/2005GL025038.

Renard, F., Mair, K., & Gundersen, O. (2012). Surface roughness evolution on experimentally simulated faults. Journal of Structural Geology, 45, 101-112.

Renard, F., Candela, T., & Bouchaud, E. (2013). Constant dimensionality of fault roughness from the scale of micro-fractures to the scale of continents, Geophysical Research Letters, 40, 83-87, doi:10.1029/2012GL054143.

Renard, F., Cordonnier, B., Dysthe, D. K., Boller, E., Tafforeau, P., & Rack, A. (2016). A deformation rig for synchrotron microtomography studies of geomaterials under conditions down to 10 km depth in the Earth. Journal of synchrotron radiation, 23(4), 1030-1034.

Renard, F., Cordonnier, B., Kobchenko, M., Kandula, N., Weiss, J., & Zhu, W. (2017). Microscale characterization of rupture nucleation unravels precursors to faulting in rocks. Earth and Planetary Science Letters, 476, 69-78.

Renard, F., Weiss, J., Mathiesen, J., Ben-Zion, Y., Kandula, N., & Cordonnier, B. (2018). Critical evolution of damage toward system-size failure in crystalline rock. Journal of Geophysical Research: Solid Earth, 123(2), 1969-1986.

Renard, F. (2020). Competition between creep and damage on faults revealed in 4D synchrotron imaging experiments [Data set]. Norstore. https://doi.org/10.11582/2020.00003.

Riedel, W. (1929). Zur Mechanik geologischer Brucherscheinungen ein Beitrag zum Problem der Fiederspatten. Zentbl. Miner. Geol. Palaont. Abt., 354-368.

Ross, Z. E., Hauksson, E., & Ben-Zion, Y. (2017). Abundant off-fault seismicity and orthogonal structures in the San Jacinto fault zone. Science Advances, 3(3), e1601946.

Ross, Z. E., Idini, B., Jia, Z., Stephenson, O. L., Zhong, M., Wang, X., Zhan, Z, Simons, M., Fielding, E., J., Yun, S.-H., Hauksson, E., Moore, A.W., Liu, Z., & Jung, J. (2019). Hierarchical interlocked orthogonal faulting in the 2019 Ridgecrest earthquake sequence. Science, 366(6463), 346-351.

Sagy, A., Brodsky, E. E., & Axen, G. J. (2007). Evolution of fault-surface roughness with slip. Geology, 35(3), 283-286.

Sagy, A., & Lyakhovsky, V. (2019). Stress patterns and failure around rough interlocked fault surface. Journal of Geophysical Research: Solid Earth, 124, 7138-7154. doi:10.1029/2018JB017006.

519 Scholz, C. H., & Engelder, J. T. (1976). The role of asperity indentation and ploughing in
520 rock friction—I: Asperity creep and stick-slip. International Journal of Rock Mechanics and
521 Mining Sciences, 13(5), 149-154.
522 Segall, P., & Pollard, D. D. (1980). Mechanics of discontinuous faults. Journal of
523 Geophysical Research: Solid Earth, 85(B8), 4337-4350.
524 Sibson, R. H. (1985). A note on fault reactivation. Journal of Structural Geology, 7(6), 751-
525 754.
526 Vermilye, J. M., & Scholz, C. H. (1999). Fault propagation and segmentation: insight from
527 the microstructural examination of a small fault. Journal of structural geology, 21(11), 1623-
528 1636.
529 Yue, H., Lay, T., & Koper, K. D. (2012). En échelon and orthogonal fault ruptures of the 11
530 April 2012 great intraplate earthquakes. Nature, 490(7419), 245-249.
531 doi:10.1038/nature11492.
532 Xu, S., & Ben-Zion, Y. (2013). Numerical and theoretical analyses of in-plane dynamic
533 rupture on a frictional interface and off-fault yielding patterns at different scales. Geophysical
534 Journal International, 193(1), 304-320.
535 Zhao, Q., Tisato, N., Kovaleva, O. and Grasselli, G. (2018). Direct observation of faulting by
536 means of rotary shear tests under X-ray micro-computed tomography. Journal of Geophysical
537 Research, 123 (9), 7389-7403.
538 Zhao, Q., Glaser, S. D., Tisato, N., & Grasselli, G. (2020). Assessing energy budget of
539 laboratory fault slip using rotary shear experiments and micro-computed tomography.
540 Geophysical Research Letters, 47, e2019GL084787. https://doi.org/10.1029/2019GL084787.
541

Table and Figures

Table 1: Experimental conditions. All experiments were performed at a temperature of 25°C, room humidity and no fluid pressure. The maximum axial stress was reached either when the experiment was stopped (sample MONZ6C) or when a secondary fault formed, leading to sample failure (other three samples). For sample MONZ8C, the confining pressure was reduced twice during the experiment because the axial loading reached the maximum capability of 200 MPa of the deformation apparatus. Initial surface roughness is 0.6 μm and 4.9 μm for smooth and rough faults, respectively.

sample name	confining pressure	maximum axial stress	total slip	# of 3D scans	fault roughness	secondary faulting
MONZ6C	40 MPa	110 MPa	2420 μm	41	smooth	No
MONZ8C	50-30-10 MPa	163 MPa	1960 μm	42	rough	Yes
MONZ9C	10 MPa	70 MPa	890 μm	5	rough	Yes
MONZ10C	10 MPa	120 MPa	1950 μm	31	rough	Yes

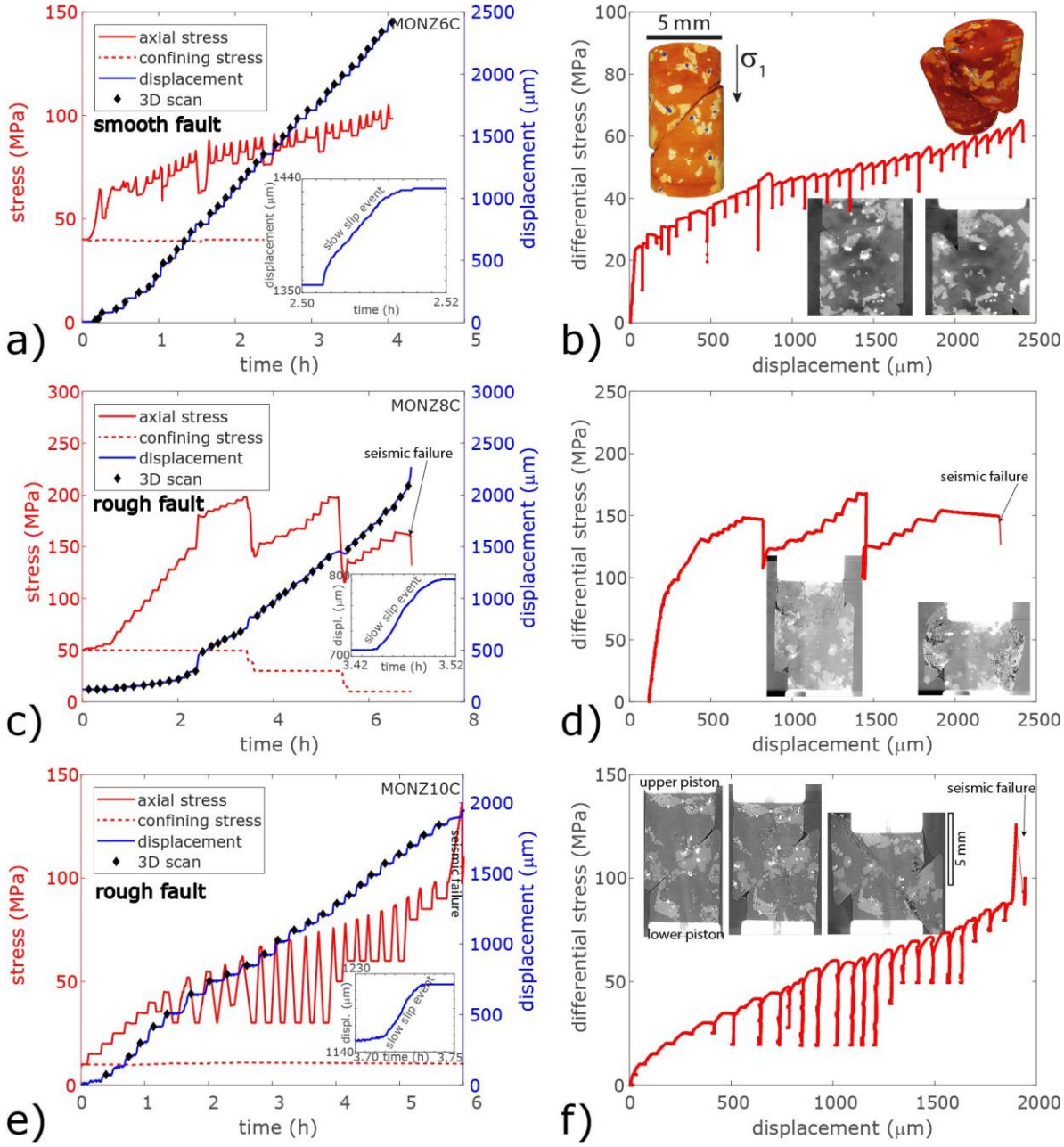

Figure 1: Experimental conditions for samples MONZ6C (a, b, see Movie S1), MONZ8C (c, d, see Movies S2, S3) and MONZ10C (e, f, see Movie S4). a, c, e) Stress conditions (left axis, red color) and displacement along the fault (right-axis, blue color) as a function of time. Each black diamond indicates the acquisition of one X-ray microtomography 3D image. Inset shows that at each stress increase, fault sliding occurred with a slow slip event. For the faults with larger roughness (c, e), the stress drop at the end of each experiment (black arrows) occurred suddenly and corresponds to a fast, presumably seismic, failure of the sample along new faults. b, d, f) Differential stress as a function of displacement along the fault. Insets

562 show either 3D views (c) or 2D views (d, f) of the saw-cut samples at different stages of slip.
563 Sample diameter is 5 mm and the saw-cut fault is oriented at 45° to σ_1. For all samples, the
564 upper and lower pistons appear as white rectangles on the 2D slices. Experiment MONZ6C
565 was performed with a smooth preexisting fault, whereas the other experiments were
566 performed on rough initial faults.

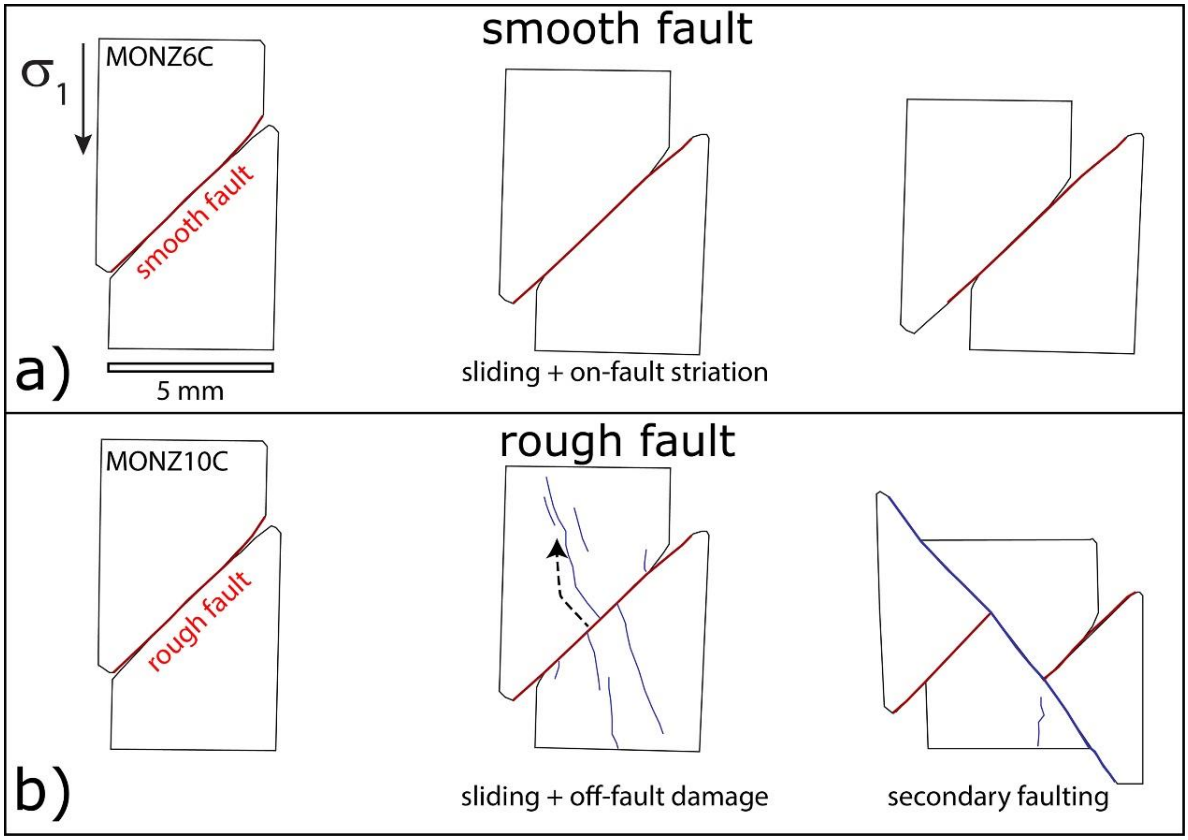

Figure 2: Cumulated slip evolution of two samples with preexisting saw-cut fault and loaded with axial stress σ_1. a) Sample MONZ6C (see Movie S1) had an initial lower fault roughness, and slipped smoothly over the full experiment, producing striations and discontinuous gouge on the fault plane. b) Sample MONZ10C (see Movie S4) had an initial larger fault roughness and slipped while damage developed in the volume surrounding the initial fault, leading to the formation of a secondary fault oriented at a high angle. Some microfractures nucleated almost perpendicularly from the fault and then their direction rotated toward the direction of the main compressive stress σ_1 (dashed arrow). Samples MONZ8C and MONZ9C, with initial rough fault, had a similar evolution as in b).

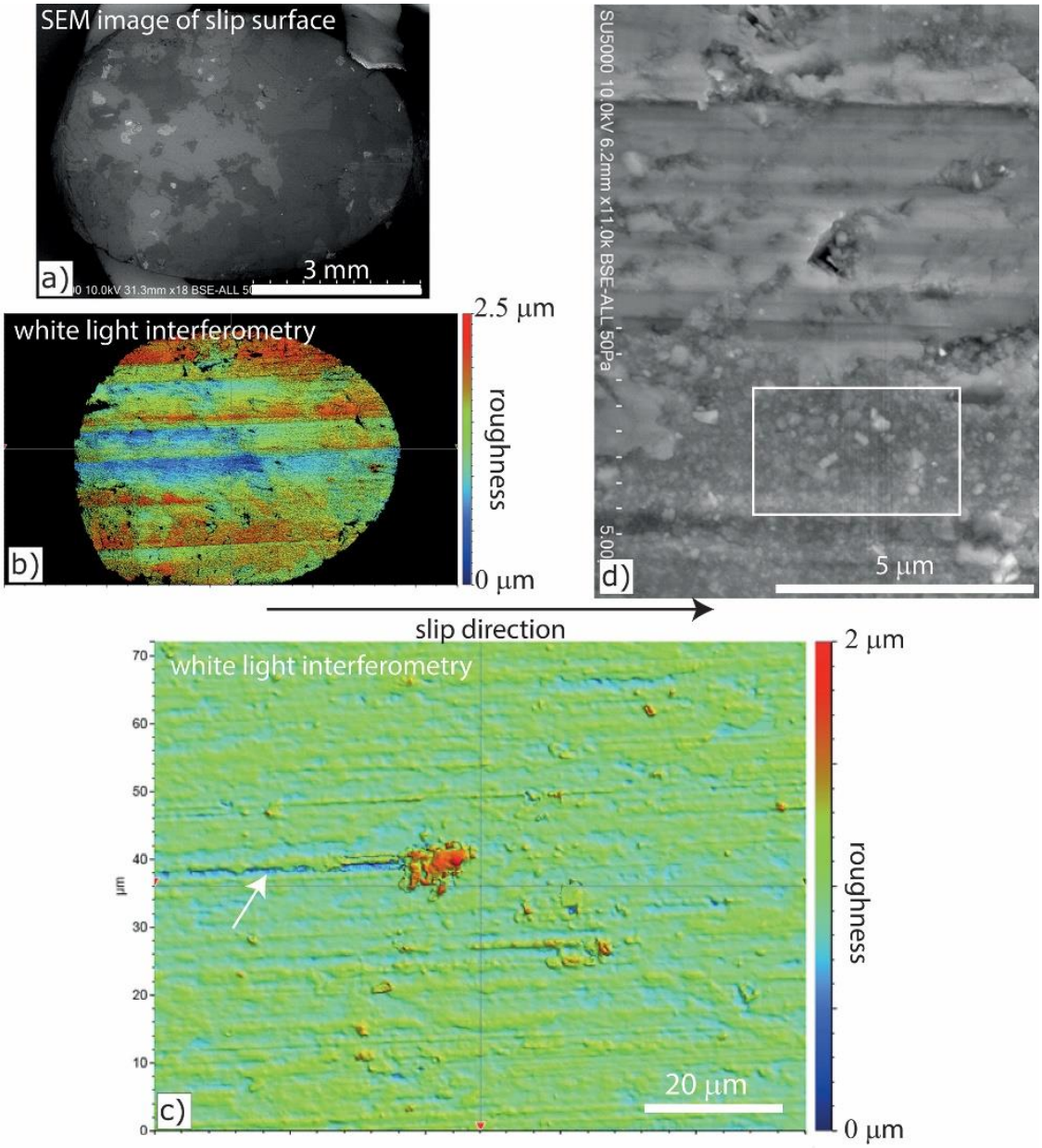

577

578 Figure 3: Slip surface of sample MONZ6C after the experiment. a) Scanning electron
579 microscope image of the entire fault surface. b, c) White light interferometry measurement of
580 surface topography and ploughing of material at the tip of striations. A white arrow marks one
581 of these striations. d) Scanning electron microscope image of the slip surface with striations
582 parallel to slip direction. Inside the white rectangle, small particles produced by wear and
583 grain comminution have accumulated in the low topography parts of the surface, forming a
584 discontinuous gouge.

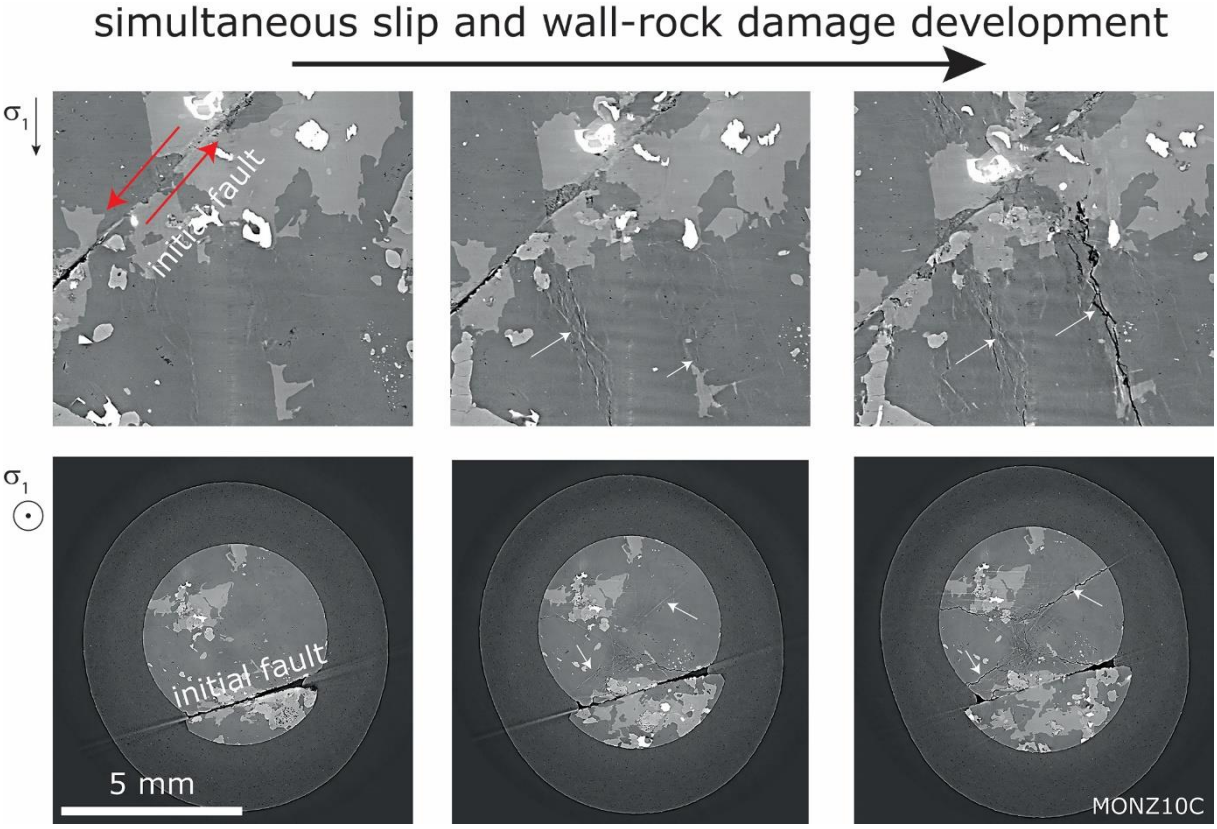

585

586 Figure 4: Two-dimensional sections in the middle of sample MONZ10C at three stages of
587 deformation showing slip along the saw-cut fault and damage development in the surrounding
588 volume. Top row: vertical sections parallel to the main compressive stress. Red arrows
589 indicate slip direction on the saw-cut fault. Bottom row: horizontal sections perpendicular to
590 the main compressive stress. Damage (white arrows) appears as cracks filled with air.

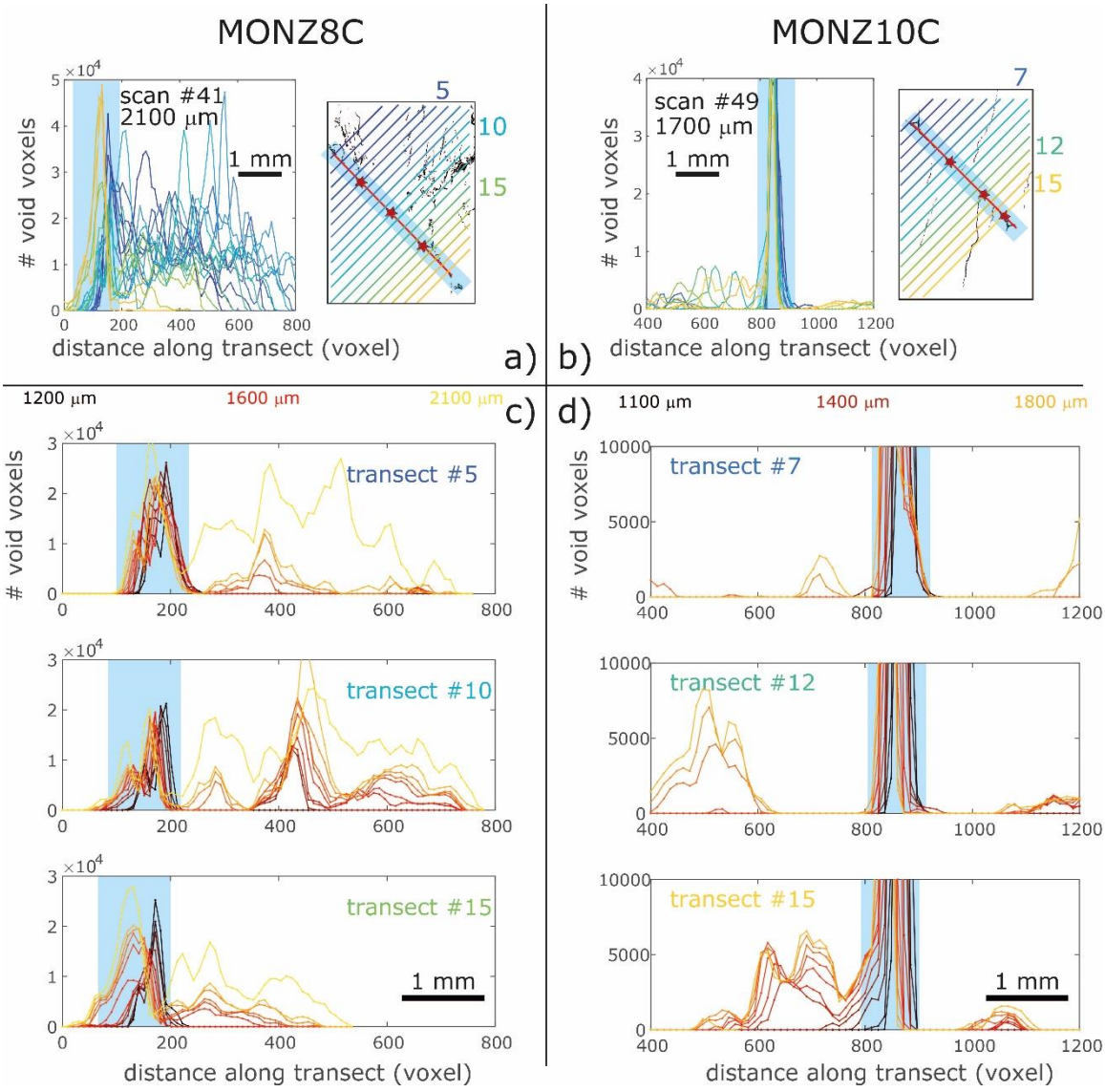

Figure 5: Distribution and evolution of wall-rock damage with slip. a, b) Number of void voxels along transects perpendicular to the fault plane in a tomogram close to failure for samples MONZ8C (after 2100 µm of slip) and MONZ10C (after 1700 µm of slip), respectively. The insets on the right side show the location of the sampling transects over two-dimensional vertical section in the sample, with the saw-cut fault in red and secondary microfractures in black. The numbers indicate transects shown in c) and d). The blue transparent rectangles highlight the region for which the number of void voxel is not representative of off-fault damage (see Section 3.3). c, d) Evolution of the number of void voxels with cumulated slip along three transects indicated in a) and b) for samples MONZ8C

and MONZ10C, respectively. The increasing number of void voxels located outside of the saw-cut fault (blue rectangles) track the development of wall-rock damage with cumulated slip.

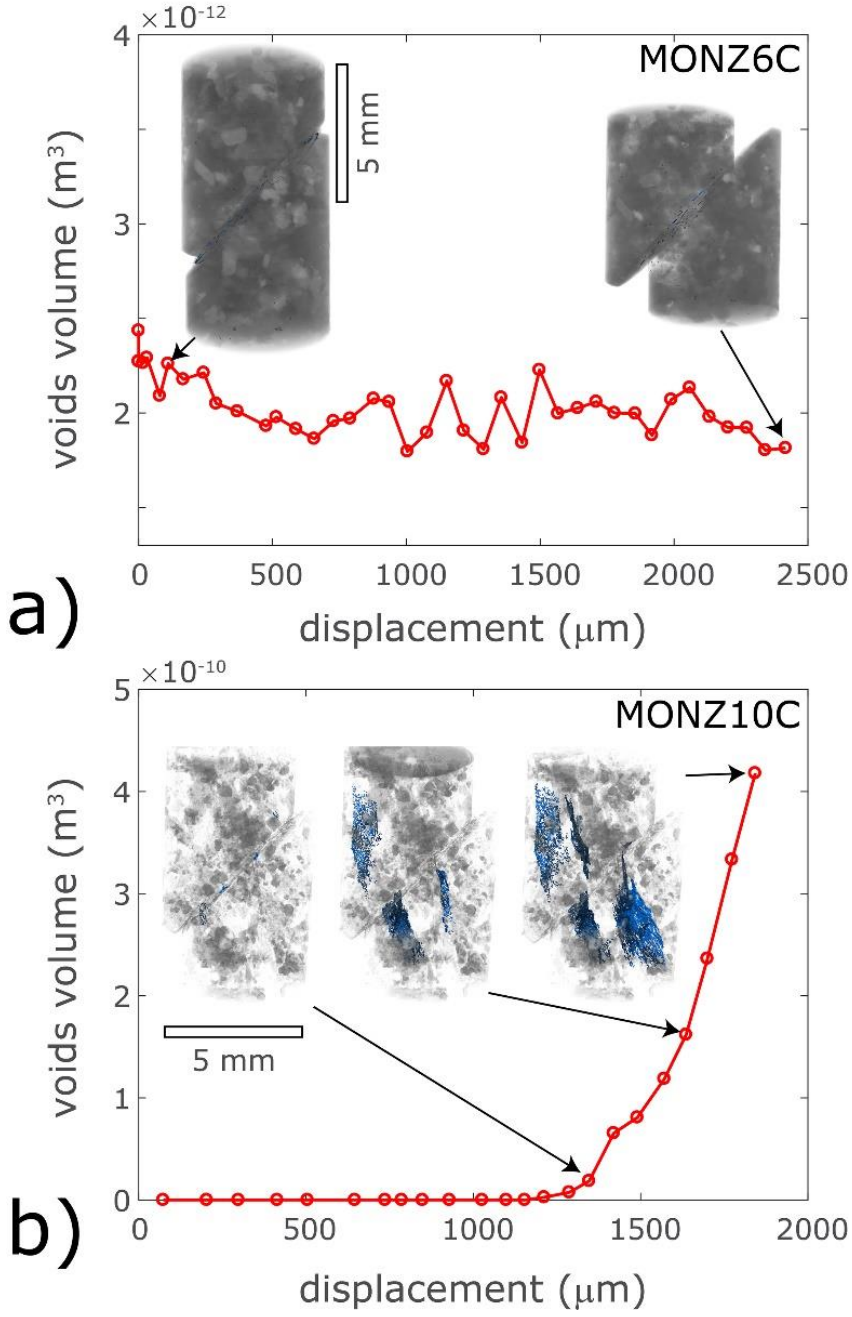

Figure 6: Evolution of voids volume, indicative of damage development, with slip. a) Smooth fault (sample MONZ6C). Voids correspond to microporosity along the fault plane and in feldspar minerals. Their volume does not vary significantly with cumulated slip. Insets: Three 3D renderings of the sample with porosity shown in blue. b) Rough fault (sample MONZ10C). Voids correspond to microfractures that open around the saw-cut fault, as well as preexisting porosity. Insets: Three 3D renderings of the sample with microfractures shown in blue and minerals in transparent gray shades.

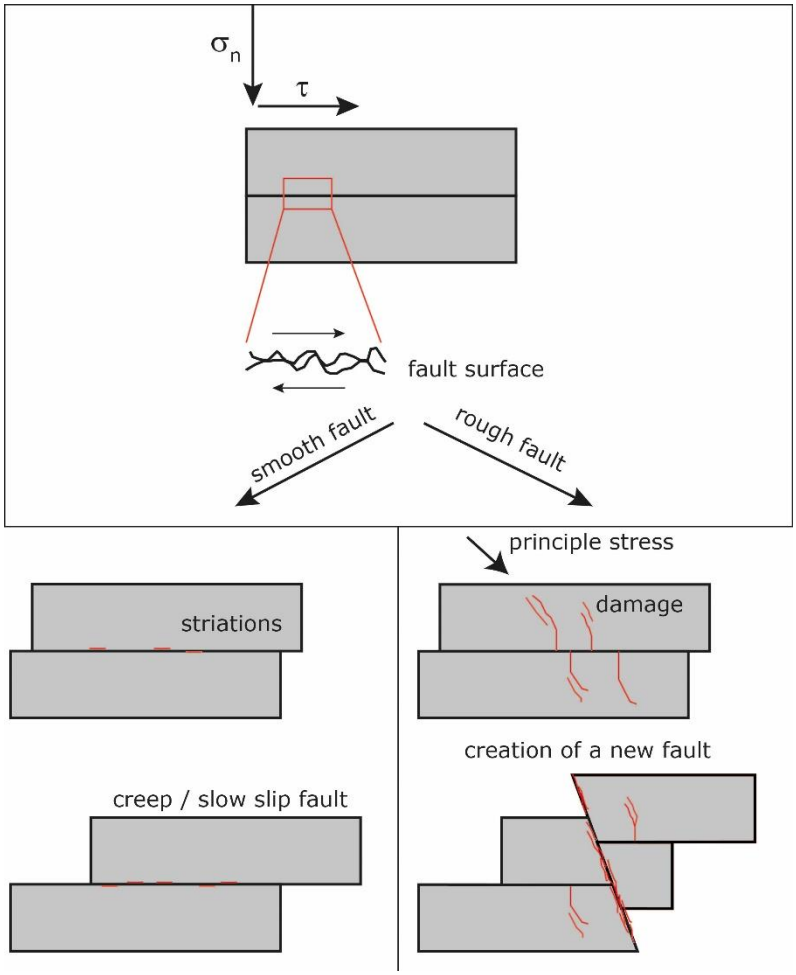

612

613 Figure 7: Dynamic X-ray microtomography experiments enable the identification of two
614 modes of slow slip and deformation along a pre-existing fault with different initial roughness.
615 A smooth fault may slide by continuous creep or slow slip events, producing striations and
616 gouge along the plane (bottom left), whereas slow slip events along a rougher fault induce
617 additional damage (red) in the surrounding volume, leading to the sudden nucleation of a
618 secondary fault oriented at a high angle (bottom right).

Supplementary Information

Competition between slow slip and damage on and off faults revealed in 4D synchrotron imaging experiments

François Renard[1,2], Jessica McBeck[1], Benoît Cordonnier[1]

[1] Physics of Geological Processes, The Njord Centre, Department of Geosciences, University of Oslo, Oslo, Norway.
[2] University Grenoble Alpes, University Savoie Mont Blanc, CNRS, IRD, IFSTTAR, ISTerre, 38000 Grenoble, France.

The supplementary information contains two figures and four movies.

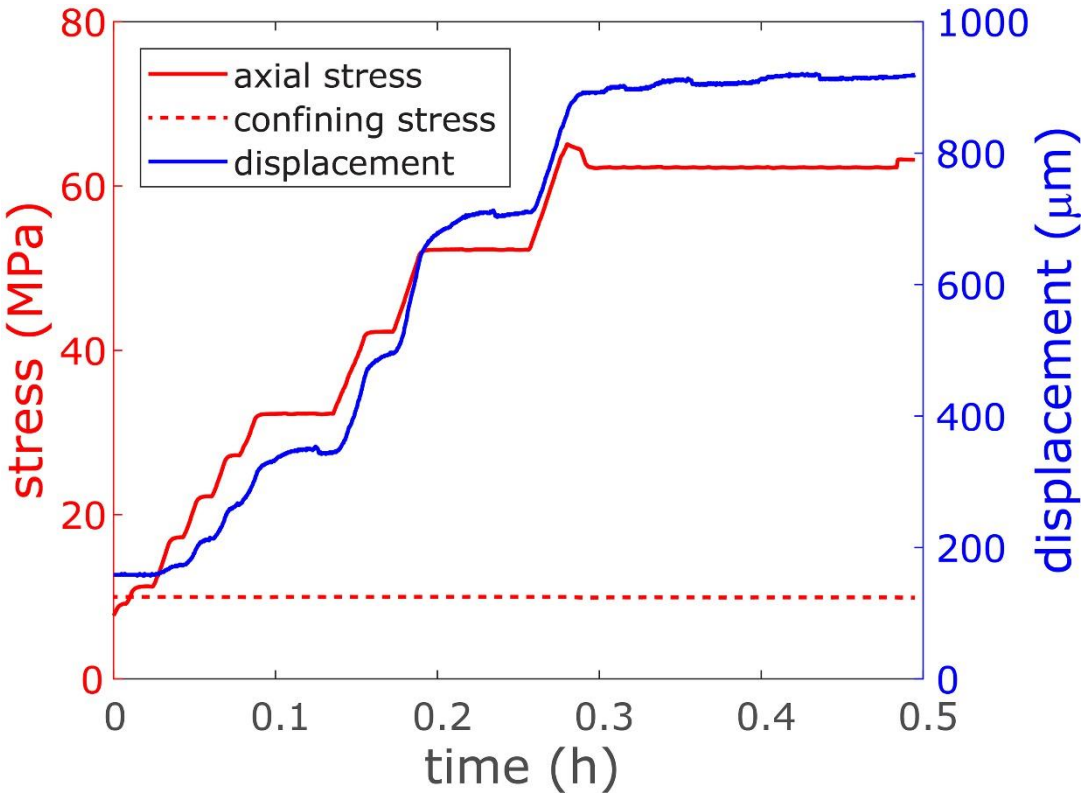

Figure S1: Experimental conditions for samples MONZ9C. Stress conditions (left axis, red color) and displacement along the fault (right-axis, blue color) as a function of time.

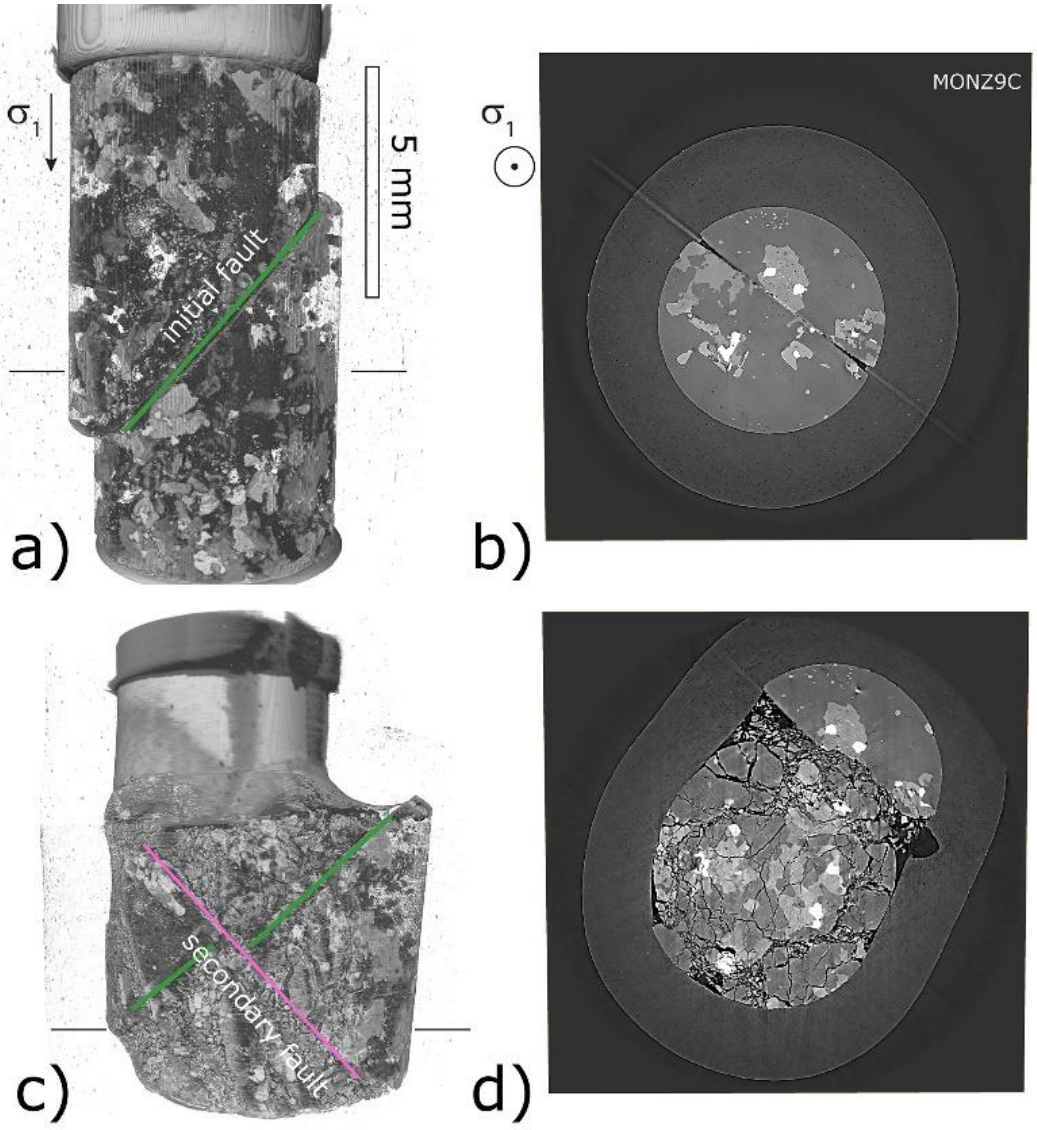

626

627 Figure S2: Three-dimensional rendering views and two-dimensional sections of sample
628 MONZ9C at two different stages of deformation. Top: At the beginning of the experiment,
629 slow slip accommodated the increase of axial loading. Bottom: Slow slip on the initial fault
630 produced damage in the surrounding volume, leading to the formation of secondary faults
631 along which sudden slip occurred. Horizontal black lines in a) and c) indicate the position of
632 the sections shown in b) and d).

633

634 Movie S1: Time evolution of slip in sample MONZ6C. Left: In this three-dimensional
635 rendering of a subvolume in the middle of the sample, the gray shades display the grains and
636 the blue color shows microporosity along the fault plane. Pores in the upper volume of the

sample move along the fault due to slip. Top right: Three-dimensional rendering of the entire sample. Bottom right: same as in Figure 1a.

Movie S2: Time evolution of slip in sample MONZ8C. Left: Three-dimensional rendering of the entire sample (false colors). Top right: A two-dimensional vertical section in the sample shows slip along the fault, the drag of some minerals in the fault plane and the formation of damage in the surrounding volume. Gray shades display X-ray attenuation with white colors corresponding to denser grains and black color corresponding to voids. Bottom right: same as in Figure 1c.

Movie S3: Three-dimensional rendering of sample MONZ8C during slip. Semi-transparent gray shades display X-ray attenuation with white colors corresponding to denser grains. The blue color displays the initial fault plane and the microfractures that develop in the volume during slow slip on the fault. The last picture shows the sample after a secondary fault has formed. Sample diameter: 5 mm.

Movie S4: Time-lapse evolution of slip on a preexisting fault in sample MONZ10C. Left: In the three-dimensional rendering of the sample, the blue color shows the initial fault plane and the microfractures that develop in the volume during slow slip on the fault. Right: A two-dimensional vertical section in the middle of the sample shows damage development during slow slip. In both panels, gray levels display X-ray attenuation with white colors corresponding to denser grains. The last picture shows the sample after a secondary fault has formed suddenly.